Nucleic Acids Research, 2025, **53**, gkaf260
https://doi.org/10.1093/nar/gkaf260
Chemical Biology and Nucleic Acid Chemistry

Oxidative events in a double helix system promote the formation of kinetically trapped G-quadruplexes

Simon Aleksič[1,2], Peter Podbevšek[1], Janez Plavec[1,2,3,*]

[1]Slovenian NMR Centre, National Institute of Chemistry, Hajdrihova 19, 1000 Ljubljana, Slovenia
[2]Faculty of Chemistry and Chemical Technology, University of Ljubljana, Večna pot 113, 1000 Ljubljana, Slovenia
[3]EN-FIST Centre of Excellence, Trg OF 13, 1000 Ljubljana, Slovenia
[*]To whom correspondence should be addressed. Email: janez.plavec@ki.si

Abstract

Guanine-rich oligonucleotide sequences can adopt four-stranded G-quadruplex structures. These sequences are highly susceptible to oxidative damage due to the low redox potential of their constituent guanine nucleotides. Oxidative lesions of guanine residue exhibit perturbations in the position of hydrogen-bond donors and acceptors, which can impair the formation of G-quadruplexes. Here we studied the effect of guanine oxidation in model systems comprised of a G-rich as well as a complementary C-rich DNA strand to discern how oxidative damage can destabilize double-stranded DNA and promote G-quadruplex formation. Our data show that G-rich strands containing oxidative lesions can still adopt the G-quadruplex fold due to the presence of spare G-tracts, which rescue the damaged G-tracts via either full or partial replacement. However, most of the observed G-quadruplexes are kinetically trapped structures and the preferred equilibrium state of the two-stranded constructs is double-stranded DNA.

Graphical abstract

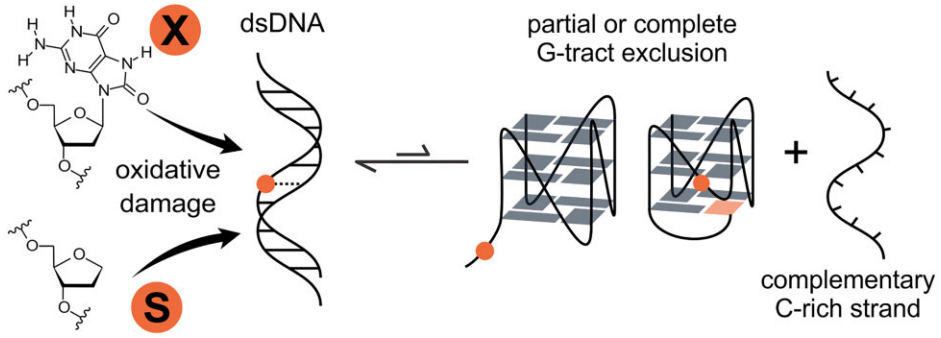

Introduction

Genomes across vertebrates, as well as lower organisms, exhibit a pattern of guanine enrichment within regions, pivotal to cellular process regulation, such as promoters and telomeres [1]. If both the G-rich and the complementary C-rich strand are available for base pairing, the formation of a stable double helix in the Watson–Crick geometry is expected. However, G-rich regions also tend to adopt a four-stranded tertiary structure known as the G-quadruplex (G4). Gene promoter regions and parts of telomeric DNA (e.g. T-loops) contain both G- and C-rich strands. Therefore, these G-rich regions are in an equilibrium between the double-stranded and the G4 tertiary structure. In complex biological systems, such as our cells, the state of equilibrium depends on the stability of the double helix and G4 in a given chemical environment at a particular point in time. The structure of a C-rich strand, which can potentially form a secondary structure of its own, the i-motif, must also be considered. However, during certain metabolic processes such as nucleic acid replication and transcription, the opening of double-stranded DNA (dsDNA) may promote G4 formation, affecting biological outcomes [2, 3]. Furthermore, the system cannot always respond instantly and shift the equilibrium toward the energetically favorable tertiary structure, as the kinetics of the transformation are limited [4]. This is especially true for the folding of complex G4s, which can involve multiple intermediates [5].

In G4s, four guanines hydrogen bond to form G-quartets stabilized by monovalent cations [6]. The sequential guanine nucleotides, known as G-tracts, are connected to each other via loops, which may assume different topologies depending

Received: December 3, 2024. **Revised:** March 17, 2025. **Editorial Decision:** March 20, 2025. **Accepted:** March 21, 2025

on the loop length and nucleotide sequence. The many possible variations in the specific orientations of the G-tracts in the G4 core and loops result in a myriad of possible topologies that can be achieved with G4s [7]. The structural polymorphism of G4s is further enriched by uncommon features such as bulges and snapbacks, which disrupt G-quartet stacking, modify loop dynamics, and impact stability or ligand recognition [8].

In addition to their structural diversity, G-rich sequences are highly susceptible to oxidative damage. Among the four common nucleotides in DNA, guanine has the lowest redox potential and is thus most vulnerable to oxidative stress, yielding an 8-oxoguanine nucleotide as a product [9]. The redox potential of guanine nucleotides is further lowered when several guanine nucleotides are positioned sequentially (i.e. in G-tracts), with only the 3′-terminal guanine nucleotide in the G-tract being significantly less susceptible to oxidation [10]. Compared to guanine, 8-oxoguanine exhibits a protonated N7 and prefers to adopt the energetically favorable *syn* conformation, due to the carbonyl group at position 8. The presence of H7 and O8 changes the arrangement of hydrogen-bond donors and acceptors on the Hoogsteen face of the 8-oxoguanine nucleobase, altering possible base-pairing geometries compared to the guanine nucleobase. Furthermore, in dsDNA the tendency of 8-oxoguanine for the s*yn* conformation promotes its base pairing with adenine, leading to a G-to-T transversion mutation. Removal of the 8-oxoguanine nucleotide from the genome is therefore crucial and is facilitated by enzymatic pathways utilizing base excision repair. The first step of the process is cleavage of the 8-oxoguanine moiety by the glycosylase OGG1, yielding an abasic site in the genome [11, 12]. Repair of the abasic site proceeds initially with the function of the human abasic endonuclease (APE1), followed by strand scission, nucleotide incorporation, and ligation via two different pathways and multiple enzymes [13].

In dsDNA, abasic sites have a destabilizing effect that reduces the thermal stability of the constructs [14]. On the other hand, the destabilizing effect of 8-oxoguanine nucleotides may be subtle because the Watson–Crick face of 8-oxoguanine remains unchanged, allowing it to form stable base pairs with cytosine while both nucleotides adopt the *anti* conformation [15, 16]. However, studies on the incorporation of 8-oxoguanine into G4-forming sequences show that the effect on the thermal stability of G4s depends on the position of the lesion in the sequence. At some positions, the 8-oxoguanine moiety can be easily incorporated into G-quartets and does induce significant structural changes despite its different hydrogen-bonding properties [17, 18]. At other positions, due to the preferred *syn* conformation, 8-oxoguanine induces major structural rearrangements in comparison to the native G4 fold [19]. As such, oxidative events in putative G4-forming sequences could affect the structure equilibrium between G4s and dsDNA.

Although four G-tracts are the norm for G4 formation, regulatory regions consistently contain multiple interspersed G-tracts, telomeric regions even numbering in the thousands [20–23]. Introduced by the Burrows Lab, these “spare” G-tracts can serve to mitigate oxidative damage via rescue of G4 structure, replacing the damaged G-tract and thus preserving G4 function under stress conditions [24]. We deemed it essential to uncover how the structural equilibrium between dsDNA and G4 is affected in a model system comprised of a G-rich strand with five G-tracts and a complementary C-rich strand.

Oxidative damage was simulated by incorporating 8-oxoguanine (**X**) and abasic (**S**) residues into the G-rich strand at positions susceptible to oxidation. We hypothesized that oxidative lesions would generally act as destabilizing agents for the DNA double helix, triggering the dynamic formation of G4 structures. However, we expected this effect to be highly dependent on the position and type of lesion. We set out to systematically map individual positions in our model system to see when the “spare tire” mechanism takes effect.

Oxidation-related shifts in molecular architecture could significantly impact genomic stability and gene regulation, opening new venues for understanding DNA damage response. Given that the interplay between G4 formation and guanine oxidation can cause disease, it is important to gain further insight into the behavior of G-rich sequences under oxidative conditions.

Materials and methods

Oligonucleotide synthesis

Oligonucleotides were synthesized on a DNA/RNA H-8 Synthesizer (K&A Laborgeräte) operating on the phosphoramidite chemistry principle. Nucleotide and dSpacer phosphoramidites were obtained from Glen Research, while isotopically labeled phosphoramidites were purchased from Cambridge Isotope Laboratories. The oligonucleotides were synthesized with the dimethoxytrityl (DMT) protecting group and deprotected for 30 min at 65°C using a 1:1 (v/v) mixture of ammonia solution and methylamine. The following purification step was carried out with Glen-Pak cartridges (Glen Research) and desalted/concentrated using 3000 MWCO Amicon centrifugal filters (Merck Millipore).

UV spectroscopy

Concentration of oligonucleotides was determined at a wavelength of 260 nm on a Cary 3500 UV spectrometer (Agilent) at 95°C. Thermal denaturation curves were obtained at 260 and 295 nm for the two-stranded constructs and single-stranded samples, respectively, from 5 to 95°C and back to 5°C, with a temperature gradient of 0.5°C/min. The DNA concentration in the melting analysis was 1.2 and 9.0 μM per strand for the two-stranded constructs and single-stranded samples, respectively. The melting curves were normalized using the minimum and maximum absorbance values of the heating and cooling curves. The first-order derivatives of the melting curves were determined using Origin 2018 software and the inflection point was selected as the melting temperature.

NMR measurements

Nuclear magnetic resonance (NMR) samples were prepared with a concentration of 0.4 mM DNA per strand, 50 mM KCl, 10 mM potassium phosphate buffer (pH 7), 10% $^{2}H_2O$ in 3- and 5-mm NMR tubes. The NMR data were acquired with Bruker Avance NEO 600 and 800 MHz spectrometers equipped with cryoprobes. 1D ^{1}H, 2D ^{1}H–^{1}H NOESY and TOCSY NMR spectra were recorded using an excitation sculpting scheme for solvent signal suppression. For NOESY experiments, the mixing times used were 80, 200, and 250 ms. For TOCSY experiments, the mixing times used were 40, 60, and 80 ms. ^{1}H–^{15}N correlations were determined by acquiring

^{15}N-HMQC spectra utilizing the SOFAST technique. Translational diffusion coefficients were determined using a DOSY experiment utilizing a stimulated echo sequence with bipolar gradients. All NMR experiments were performed with a relaxation delay of 1.5 s. Samples were either quenched (heated to 95°C for 2 min and snap-cooled on ice) or annealed (heated to 95°C for 2 min and cooled to 25°C over 12 h) prior to NMR measurements. The spectra were processed and analyzed with the software packages TopSpin, SPARKY, and MestReNova.

Circular dichroism

Circular dichroism (CD) spectra were obtained on a Chirascan CD spectrometer (Applied Photophysics) at 25°C in 10 parallel measurements from 200 to 320 nm in a 0.1 mm cell length cuvette. The DNA concentration was 27 μM with the same buffer as used for NMR. Parallel measurements were averaged and smoothed using a Savitzky–Golay filter with a window size equal to 5.

Structural prediction

The predictions of the g2S, g10S, and g19S G4 structures were generated using the AlphaFold 3 model [25] and validated against NMR data for structural accuracy.

Results

Alternating loop length strongly affects the dsDNA:G4 equilibrium

In order to determine the effect of oxidative damage on the dsDNA:G4 equilibrium, we first set out to develop a model system, where dsDNA and G4 structures would coexist at selected *in vitro* conditions. Such a system requires a G-rich strand with thymine loops and a fully complementary C-rich strand with adenines. In the G-rich strand, we opted for G-tracts with three guanine nucleotides, which are common in many genomic G4-forming sequences. Furthermore, uniform length of the G-tracts diminishes the possibility of register shifting, which reduces structural polymorphism. G-rich strands contained five G-tracts to allow for exclusion of a damaged G-tract and the maintenance of the G4 structure. For simplicity, loops were comprised solely of thymine nucleotides.

Initially, G-rich strands contained loops of uniform length, i.e. T, TT, and TTT, named mL1, mL2, and mL3, respectively (Fig. 1A and Supplementary Table S1). The samples were quenched by heating to 95°C and denaturing the DNA, followed by rapid snap cooling on ice. The presence of dsDNA and G4 structures was established by analyzing 1D ^{1}H NMR spectra (Fig. 1B). Characteristic resonances were observed in the imino region for Watson–Crick base pairs of dsDNA (δ 12–14 ppm) and Hoogsteen hydrogen-bonded guanines of G4s (δ 10–12 ppm). However, no imino resonances of protonated cytosines could be observed at around δ 15 ppm, which would indicate the formation of i-motif structures.

In the case of mL1, most of the G-rich strand (in the presence of a fully complementary 19-nt C-rich strand) folded into a G4 structure, while only a negligible fraction formed dsDNA (Fig. 1B). The situation was reversed with mL2 forming predominantly dsDNA and only a small fraction of G4. The mL3 two-stranded constructs exhibited exclusively dsDNA. Our experiments have shown that loop length is a decisive factor influencing population ratios of the dsDNA:G4 equilibrium in our two-stranded constructs at specific conditions.

With further fine-tuning of the loop lengths, we sought to obtain a model system with a balanced distribution of dsDNA and G4 populations. This led to the design of a G-rich strand (gLV) with alternating loop lengths of TT and T, paired with a complementary C-rich strand (cLV). The resulting two-stranded constructs were designated as mLV (Fig. 1C). Immediately after quenching, the ^{1}H NMR spectrum of mLV gave rise to several sharp resonances in the δ 10–12 ppm range, indicating the formation of a G4 with a well-defined topology (Fig. 1D). Additionally, a broad signal envelope was observed in the Hoogsteen region at δ 11 ppm, indicating either multiple structures in solution or aggregated higher-order structures. Further downfield in the ^{1}H NMR spectrum, two sets of signals corresponding to GC (δ 12.6–13.2 ppm) and AT (δ 13.6–14.0 ppm) base pairs were observed, confirming the formation of dsDNA. Based on the imino signal intensities, mLV in solution demonstrates a roughly 1:1 ratio of dsDNA and G4 structures (Fig. 1D). However, the intensity of imino resonances associated with G4 decreases with time, suggesting that G4 is a kinetically trapped structure that converts into a thermodynamically preferred dsDNA. After 16 h at room temperature, resonances associated with G4 are reduced to around 30% of the original intensity. The broad envelope at δ 11 ppm persists even after 16 h and does not seem to change with time. Interestingly, despite the neutral pH, NMR spectra of mLV contained broadened low-intensity signals at approximately δ 15.5 ppm, indicating that a fraction of the C-rich strand, which is not hybridized with the G-rich strand, adopts the i-motif structure (Fig. 1D).

To account for the differing folding kinetics of dsDNA and G4 structures, mLV was also annealed by heat denaturing the DNA followed by cooling the solution overnight using a linear temperature gradient (Fig. 1D). In this case, no well-resolved imino resonances could be observed in the Hoogsteen spectral region, except for the broad envelope at δ 11 ppm. Nevertheless, given the comparable populations of dsDNA and G4 observed after quenching, mLV was chosen as the model system for further analysis of the effect of oxidative lesions on the structural equilibrium.

The position of the oxidative lesion in the sequence controls the equilibrium

We individually replaced the guanine nucleotides thought to be susceptible to oxidation in gLV with 8-oxoguanine (**X**) and dSpacer residues (**S**). Independently, all G-rich strands were found to form G4 structures with spectral quality ranging from well-resolved, sharp NMR resonances to poorly dispersed, broad signals (Supplementary Figs S1 and S2). Equimolar mixtures of gLV strands with oxidative lesions and the unmodified cLV strand were quenched and annealed separately. The resulting two-stranded constructs were named with the position and type of lesion in the G-rich strand (e.g. m19X represents a two-stranded construct with **X** at position 19). ^{1}H NMR spectra were used to determine the presence and populations of dsDNA and/or G4 structures in each two-stranded construct (Supplementary Figs S1 and S2). Two-stranded constructs with **X** in the central three G-tracts (m6X, m7X, m10X, m11X, m15X, and m16X) hybridized mostly into dsDNA after quenching with signals in the δ 12.6–14.0 ppm range (Supplementary Figs S1 and S3). Only broad low-

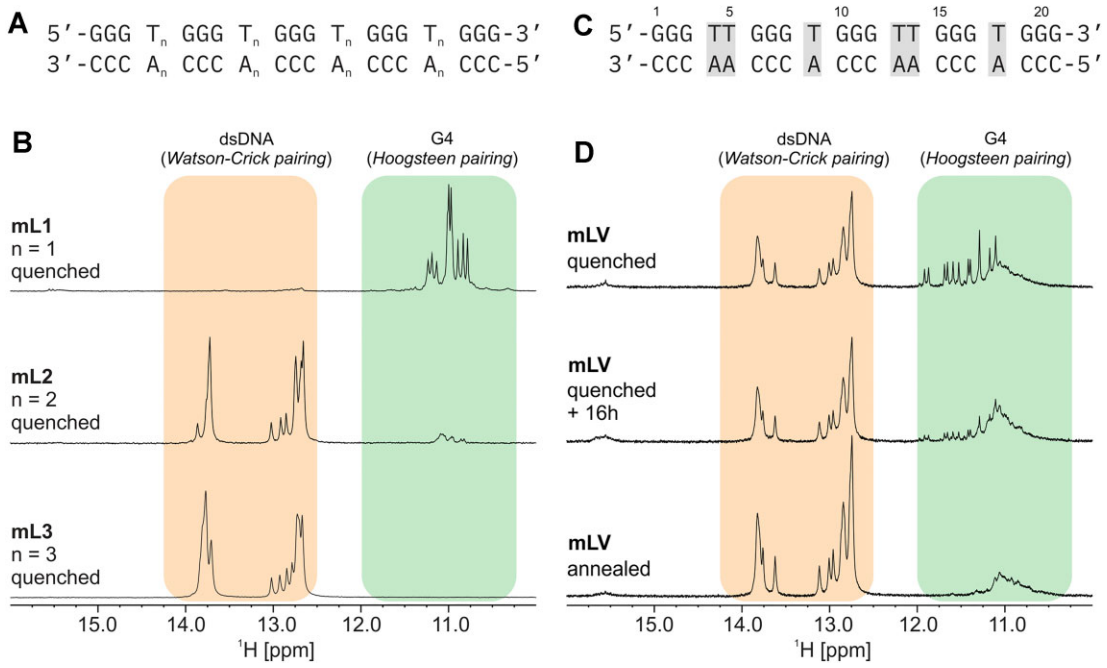

Figure 1. Designing a model system for observing the dsDNA:G4 equilibrium. (**A**) Sequences of the two-stranded constructs with varying loop lengths. (**B**) Imino regions of ^{1}H NMR spectra for three two-stranded constructs with uniform loop lengths, ranging from one to three thymines. Watson–Crick and Hoogsteen bonded imino regions are highlighted. (**C**) Sequences of the two oligonucleotides forming the mLV two-stranded constructs. Loops are shaded and the G-rich strand is labeled numerically. (**D**) Imino region of ^{1}H NMR spectra of the mLV two-stranded constructs after sample quenching, quenching and waiting for 16 h, and annealing. Spectra were recorded at 25°C on 800 and 600 MHz NMR spectrometers with a 0.4 mM DNA concentration (per strand), 50 mM KCl, 10 mM potassium phosphate buffer (pH 7), and 10% $^{2}H_2O$.

intensity signals were observed in the δ 10.8–12.2 ppm range, which would indicate G4 formation. On the other hand, we observed the formation of both dsDNA and G4 structures for two-stranded constructs with **X** in the 5′-G-tract (i.e. m1X and m2X) and in the 3′-G-tract (i.e. m19X and m20X). After quenching, the G4 population in m1X and m2X amounted to around 55% and 50%, respectively (Fig. 2). In m19X and m20X, the integrals of the signals belonging to G4 were lower, amounting to a G4 population of ∼25%. In comparison, all two-stranded constructs with **X** in the G-rich strand, when annealed for 12 h, showed imino signals belonging to dsDNA and only broad low-intensity envelopes in the G4 fingerprint region. Most G4 formation was observed in m1X with ∼20% population after annealing (Supplementary Fig. S3). As with all **X**-containing two-stranded constructs after annealing, the G4 fingerprint imino region of the ^{1}H NMR spectra of m1X exhibited a broad envelope indicating that the G4s did not adopt a single well-defined structure (Supplementary Fig. S3).

In all **X**-containing two-stranded constructs, the opposite position to **X** is a C and the two can form a Watson–Crick base pair. However, **X** prefers the *syn* conformation, which is incompatible with the opposing C as it favors base pairing with A. In our two-stranded constructs, the *syn* conformation of **X** is expected to destabilize dsDNA, potentially promoting G4 formation. In an attempt to tune the equilibrium, we prepared two-stranded constructs of g1X, g2X, g19X, and g20X with complementary C-rich strands containing A opposite **X** (Supplementary Table S1). The parent m1X and m2X exhibited a high G4 population after quenching and their C to A mutants (m1X-C21A and m2X-C20A) showed a significant shift in the structural equilibrium toward dsDNA (Supplementary Fig. S4). Conversely, other parent two-stranded constructs with initially low G4 populations showed negligible differences in the dsDNA:G4 equilibrium upon introduction of C to A mutants.

Quenching of two-stranded constructs with **S** in the 5′-G-tracts (m1S and m2S) and in the 3′-G-tracts (m19S and m20S) resulted in the formation of both dsDNA and G4 structures. The population of G4 was around 45% and 60% for m1S and m2S, respectively (Supplementary Figs S5 and S6). In m19S and m20S, the G4 population amounted to ∼30% (Fig. 2). Interestingly, quenching of m10S also resulted in a significant 25% population of the G4 structure with respect to the dsDNA, giving rise to well-resolved imino resonances (Supplementary Fig. S5). Lower populations (∼10%) of G4s were also detected for other two-stranded constructs with **S**, namely m6S and m11S. After annealing, two-stranded constructs with **S** strongly favored dsDNA in all but the 3′-G-tract and only small populations of G4s could be detected in the ^{1}H NMR spectra (Fig. 2 and Supplementary Fig. S5). These experiments were designed to assess the overall impact of **X** and **S** on the dsDNA:G4 equilibrium. In the context of longer dsDNA, the G4 form is expected to be disfavored. For instance, T_5 (and complementary A_5) extensions on 5′, 3′, or both ends of m10S shift the structural equilibrium completely toward the dsDNA form (Supplementary Figs S7 and S8).

On the other hand, the annealing of the two-stranded constructs with **S** in the 3′-G-tract resulted in a higher percentage of G4 formation in the case of m19S. The G4 population was estimated to be at around 55% and 20% for m19S and m20S, respectively.

We attempted to shift the structural equilibrium in m2S, m10S, and m19S in favor of dsDNA by adding a two-fold mo-

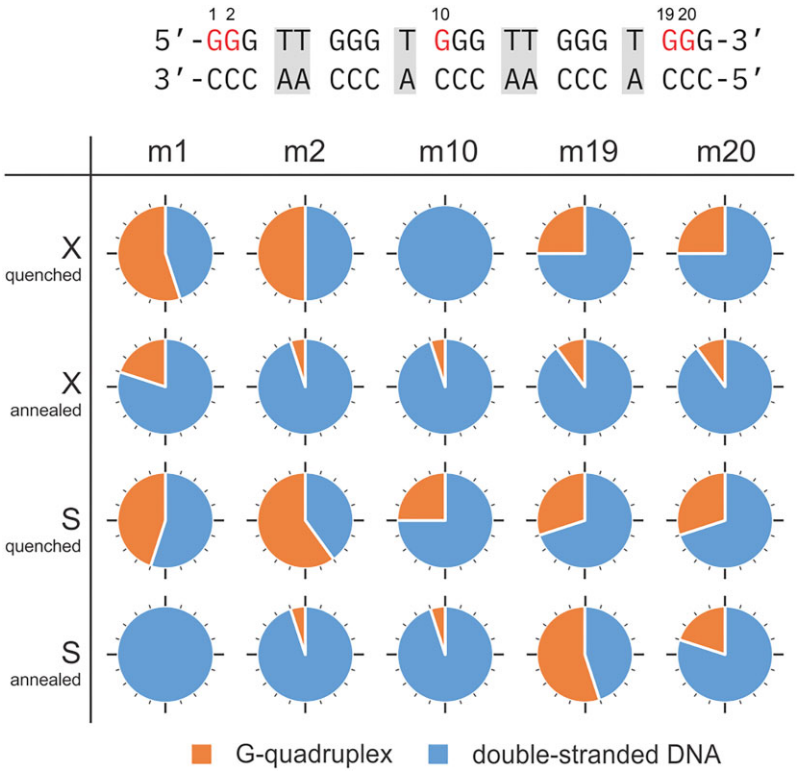

Figure 2. Population distribution in the selected two-stranded constructs. The names are defined by combining the top row and the left column. The pie charts show the population percentages of dsDNA and G4 structures. The population distributions are grouped according to the lesion position in the sequence, lesion type, and folding protocol. Thin and bold tick marks denote the population percentages in increments of 5% and 25%, respectively.

lar excess of corresponding C-rich strands (Supplementary Table S1). The equilibrium significantly shifted toward dsDNA in all samples (Supplementary Fig. S9). However, high populations of G4 in m2S and m19S persisted after quenching, while in m10S it dropped to the detection limit.

In an alternative approach to convert dsDNA to G4, we began with m19S annealed in the presence of 50 mM LiCl. As expected, the initial ^{1}H NMR spectrum indicated that the dsDNA form was predominant (Supplementary Fig. S10). However, a low-intensity, broad signal envelope was observed in the Hoogsteen spectral region, likely reflecting nonspecific G:G interactions. The analysis of the population distribution estimates the presence of G4 at around 20%. To shift the equilibrium toward G4, we titrated the sample with a concentrated KCl solution, incrementally adding up to 2 equiv. relative to LiCl, without increasing the temperature. Upon KCl addition, sharp resonances appeared in the Hoogsteen imino region of the ^{1}H NMR spectrum, consistent with those observed following thermal annealing of m19S (Supplementary Fig. S10). The G4 population was estimated to be 25% with 0.5 equiv. of KCl and remained unchanged with further additions of KCl up to 2 equiv. For comparison, quenching or annealing m19S resulted in 30% and 55% of G4 populations, respectively.

Oxidative lesions leading to the highest percentage of G4 with well-resolved imino resonances are in the first, third, or fifth G-tract of two-stranded constructs (Figs 2 and 3A). Comparison of NMR resonances in the fingerprint Hoogsteen region (δ 11.0–12.2 ppm) enabled us to cluster two-stranded constructs with identical resonance patterns into groups corresponding to a specific G4 fold (Fig. 3B). The first group consists of m1X, m2X, m1S, and m2S, which exhibit 12 Hoogsteen imino resonances corresponding to three G-quartet planes. The second group includes only m10S, which also displays 12 imino resonances but with a distinct resonance pattern. The last group consists of m19X, m20X, m19S, and m20S with partially resolved upfield-shifted (δ 10.8–11.3 ppm) imino resonances (Fig. 3B). However, their broad linewidths and poor chemical shift dispersion suggest G4 multimerization [26, 27].

Given the shared spectral features of two-stranded constructs, we found it worthwhile to characterize three representative G4 structures in detail (Table 1). Initially, we tested whether the presence of complementary C-rich strands affects the G4 structure of m2S, m10S, and m19S.

We found this not to be the case with (G-rich only) g2S, g10S, and g19S exhibiting Hoogsteen imino resonance patterns identical to their corresponding two-stranded constructs (m2S, m10S, and m19S) (Fig. 3B and C). Due to better spectral properties, we decided to use only the G-rich strands for a detailed structural analysis.

Oligonucleotide g2S with a lesion in the first G-tract forms a parallel G4 by utilizing the spare tire principle

The CD spectrum of g2S showed characteristic maxima at 210 and 265 nm and a minimum at 245 nm, suggesting that it formed a parallel topology (Supplementary Fig. S11). g2S contains **S** in the first G-tract, which can be excluded from the G4 core, while the remaining four G-tracts form the G4 structure. Identification of the Gs involved in G-quartet formation was made by individual position-specific ^{15}N enrichment (Supplementary Fig. S12). Gs of the second, third, fourth,

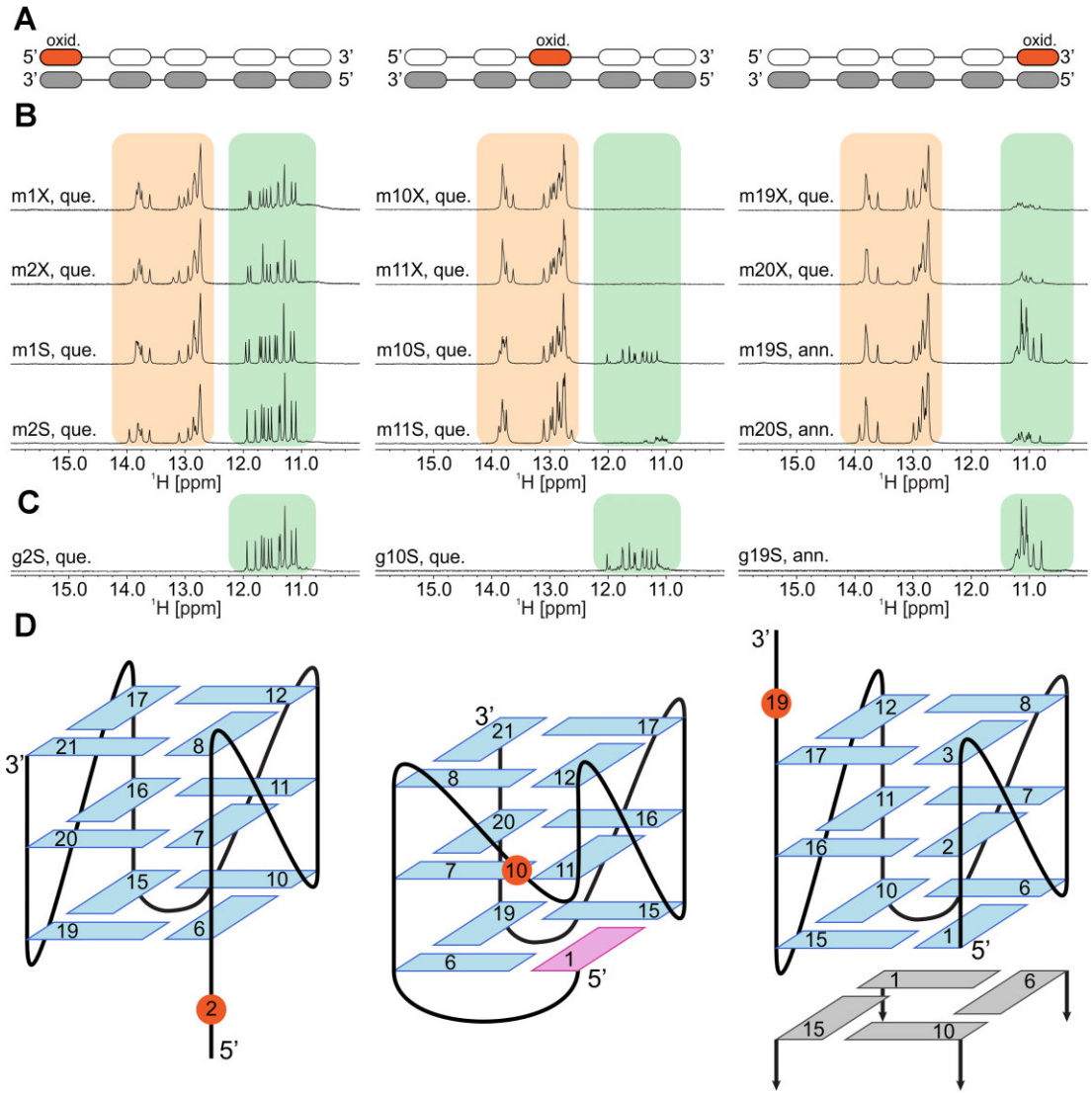

Figure 3. Position of oxidative lesion leads to formation of distinct G4 structures. (**A**) Schematic representation of selected two-stranded constructs. G-tracts containing the oxidative lesion are colored orange. The complementary C-rich strand is shaded gray. (**B**) Imino region of ^{1}H NMR spectra of the two-stranded constructs. The spectral regions signifying Watson–Crick and Hoogsteen base-paired protons are shaded in orange and green, respectively. DNA concentration was 0.4 mM (per strand) with 50 mM KCl, 10 mM potassium phosphate buffer (pH 7), and 10% ^2H_2O. Spectra were recorded at 25°C on a 600 MHz NMR spectrometer. (**C**) Imino region of ^{1}H NMR spectra of only G-rich strands containing an oxidative lesion. (**D**) Schematic representation of G4 topologies of g2S (left), g10S (middle), and g19S (right). Magenta and blue colors represent *syn* and *anti* nucleotides, respectively. The oxidative lesion position is marked with an orange circle. Thymine and guanine nucleotides not involved in G-quartets are omitted for clarity. In the case of the g19S dimer, the second G4 is shown schematically.

Table 1. Selected oligonucleotides and their sequences

Construct name	Nucleotide sequence
g2X	5′-GXG TT GGG T GGG TT GGG T GGG-3′
g2S	5′-GSG TT GGG T GGG TT GGG T GGG-3′
g10X	5′-GGG TT GGG T XGG TT GGG T GGG-3′
g10S	5′-GGG TT GGG T SGG TT GGG T GGG-3′
g19X	5′-GGG TT GGG T GGG TT GGG T XGG-3′
g19S	5′-GGG TT GGG T GGG TT GGG T SGG-3′

and fifth G-tracts gave rise to imino resonances in ^{15}N-edited HMQC spectra, while G1 and G3 did not. We unambiguously assigned NOE cross-peaks in the aromatic–anomeric region of the NOESY spectrum of g2S and traced a sequential walk throughout the sequence with interruptions at T9, T13, and T18 (Supplementary Fig. S13). Observation of the G1H1′–G3H8 cross-peak in the NOESY spectrum (Supplementary Fig. S13) indicated spatial proximity of the G1 and G3 and suggested stacking of their nucleobases. Imino–aromatic NOE cross-peak assignment allowed us to establish H1–H8 connectivities within the three G-quartets, which were in agreement with the parallel G4 topology. Based on intra-nucleotide H1′–H8 cross-peak intensities, all Gs involved in G-quartet formation were assigned the *anti* N-glycosidic bond conformation (Supplementary Fig. S13). We further determined the thermal stability of the g2S G4 using UV and measured a melting temperature of 86°C (Supplementary Fig. S14). Interestingly, the thermal stability of the G4 was noticeably higher than that of the mLV two-stranded constructs, which exhibited a melting temperature of 65°C (Supplementary Fig. S15).

The structure of g2S was predicted with AlphaFold 3 and was found to be consistent with the NMR data. All 3D structural models exhibit a parallel G4 core with propeller loops, while the 5′ overhangs, including the displaced G-tract and loop (G1–T5), form a capping structure (Supplementary Fig. S16). This structure is in agreement with the G1H1′–G3H8 cross-peak observed in NOESY spectra. Comparable results were obtained regardless of the absence of K^+ cations or the inclusion of 2 or 20 K^+ cations. In particular, two cations were consistently positioned correctly between two neighboring G-quartet planes.

The g10S G4 partially replaces the third G-tract

Initially, we anticipated that g10S adopts a G4 fold where the third G-tract is simply excluded from the G4 core, resulting in an elongated propeller loop bridging the second and fourth G-tracts. However, ^{15}N-edited HMQC spectra revealed that G1, G11, and G12 were involved in the G4 core formation (Supplementary Fig. S17). On the other hand, no imino resonances of G2 and G3 could be observed in ^{15}N-edited HMQC spectra, suggesting that the first G-tract only partially contributes to G-quartet formation (Supplementary Fig. S17). Despite characteristic CD bands suggesting a parallel G4 topology, an observable shoulder in the region from 280 to 300 nm indicated the presence of base stacking different from the *anti–anti* step (Supplementary Fig. S11) [28]. In the NOESY spectrum, the intra-nucleotide H8–H1′ NOE cross-peak of G1 exhibited a higher intensity in comparison to the corresponding cross-peaks of other Gs, indicating that G1 adopts the *syn* conformation (Fig. 4A). In addition, we were able to observe a nonsequential G1H1′–G11H8 NOE cross-peak, suggesting spatial proximity of the two nucleotides. The sequential walks were traced for segments G1–T9, G11–G12, and G19–G21 (Fig. 4A). The G8H1′–T9H8 NOE cross-peak suggests that the adjacent propeller loop (T9–S10) is less spatially constrained, as the two-nucleotide loop essentially only spans two G-quartets. The sequential walk is interrupted at position 10 (due to **S** lacking the aromatic proton) and at T13 and T18, which constitute the propeller-type loops. A sequential walk from T14 to G17 could not be traced due to severe resonance overlap. Connectivities between nucleotides in G-quartets were further confirmed via analysis of the imino–aromatic region of the NOESY spectrum. A combined analysis of NMR data shows that g10S adopts a 5′-snapback topology where G1 takes up the abasic residue's position in the central G-tract (Fig. 4B). The melting temperature of g10S G4 is 67°C (Supplementary Fig. S14).

G4 structure of g10S exhibits a 5′-snapback topology

We compared our proposed topology with structures obtained from the AlphaFold 3 server, which failed to reliably predict the snapback topology of g10S. In the presence of K^+ cations (either 2 or 20), the algorithm consistently generated G4-like tetrahelical structures with a spiral arrangement of guanine nucleobases that do not form planar G-quartets.

However, in the absence of K^+ cations, ∼10% of the predicted models (5 out of 50) agreed with NMR data (Fig. 5A). The 12 guanines involved in G-quartet formation were identified by ^{15}N-edited HMQC spectra, while G2 and G3 were not part of the G-quartets. Instead, G2 and G3, along with the adjacent T4 and T5, form an edgewise loop connecting G1 to the second G-tract. G1 adopts the *syn* conformation, occupying the G-quartet vacancy created by S10 (Fig. 5B). A propeller loop formed by T9 and S10 spans from G8 to G11, linking the two adjacent G-quartets. Additional propeller loops connect the second, third, and fourth G-tracts. In the cluster of five structures, all G-quartet positions align with the NOE connectivities observed in the NOESY spectrum of g10S (Fig. 4).

Overhangs prevent g19S dimer formation

CD spectra of g19S exhibited characteristic maxima at 210 and 265 nm and a minimum at 245 nm, which suggested a parallel topology (Supplementary Fig. S11). All G nucleotides from G1 to G17 gave rise to imino resonances in ^{15}N-edited HMQC spectra, while G20 and G21 did not, exclusion of the final G-tract from G-quartet formation (Supplementary Fig. S18). Despite considerable overlap in the aromatic–anomeric region of the NOESY spectrum, sequential walks could be traced between G1–G3, G10–G12, and G15–G21 (Supplementary Fig. S19A). Poorly dispersed aromatic resonances around δ 7.8 ppm were assigned to T5, T9, and T14, along with G1, G6, G10, and G15, which are part of the 5′-terminal G-quartet. The T18H1′–G20H8 NOE cross-peak indicates proximity of the two nucleotides, possibly due to favorable stacking of T18 and G20 nucleobases. The G20H1′–G21H8 NOE cross-peak was of lower intensity, which may be due to the flexibility of the 3′ overhang. Overlap of aromatic resonances of T4, T5, T13, and T14 prevented a comprehensive NOE analysis. However, intra-nucleotide NOE cross-peak intensities suggest that all nucleotides are in the *anti* conformation. The connectivities in the imino–aromatic region of NOESY spectra corroborated the parallel G4 topology (Fig. 3D and Supplementary Fig. S19B).

The upfield-shifted imino resonances of g19S, in the δ 10.5–11.2 ppm range, suggest dimer formation (Supplementary Fig. S19C). 5′–5′ end stacking of two g19S units seemed plausible. We tested this hypothesis by adding additional non-G nucleotides to the 5′-terminus to disrupt dimerization. The addition of a single thymine overhang (Tg19S) resulted in a new set of well-resolved imino resonances in the δ 11.0–11.9 ppm region, which was indicative of a new monomeric species (Supplementary Fig. S20). However, dimerization was only partially disrupted as a set of imino resonances assigned to the dimer could still be observed. Therefore, another thymine was added to the 5′ overhang (TTg19S), which finally disrupted dimerization as only 12 well-resolved imino resonances of the monomer were observed in the ^{1}H spectrum of TTg19S (Supplementary Fig. S20). We corroborated the mono- and dimeric nature of species by measuring translational diffusion coefficients (D_t) in a set of DOSY experiments (Table 2). Multiple well-resolved NMR resonances in the aromatic region were used for the calculation of average D_t values (Supplementary Fig. S20). The fast-diffusing monomeric species and slower-diffusing dimeric species observed in Tg19S were fully consistent with the monomeric species of g19S and the dimeric species of TTg19S, respectively (Table 2).

The g19S G4 exhibits a melting temperature of 80°C, which is concentration dependent (Supplementary Figs S14 and S21). Notably, the melting curve does not show a distinct transition indicative of dimer-to-monomer conversion. This absence could be attributed to the lower oligonucleotide concentration used in UV melting studies compared to NMR conditions,

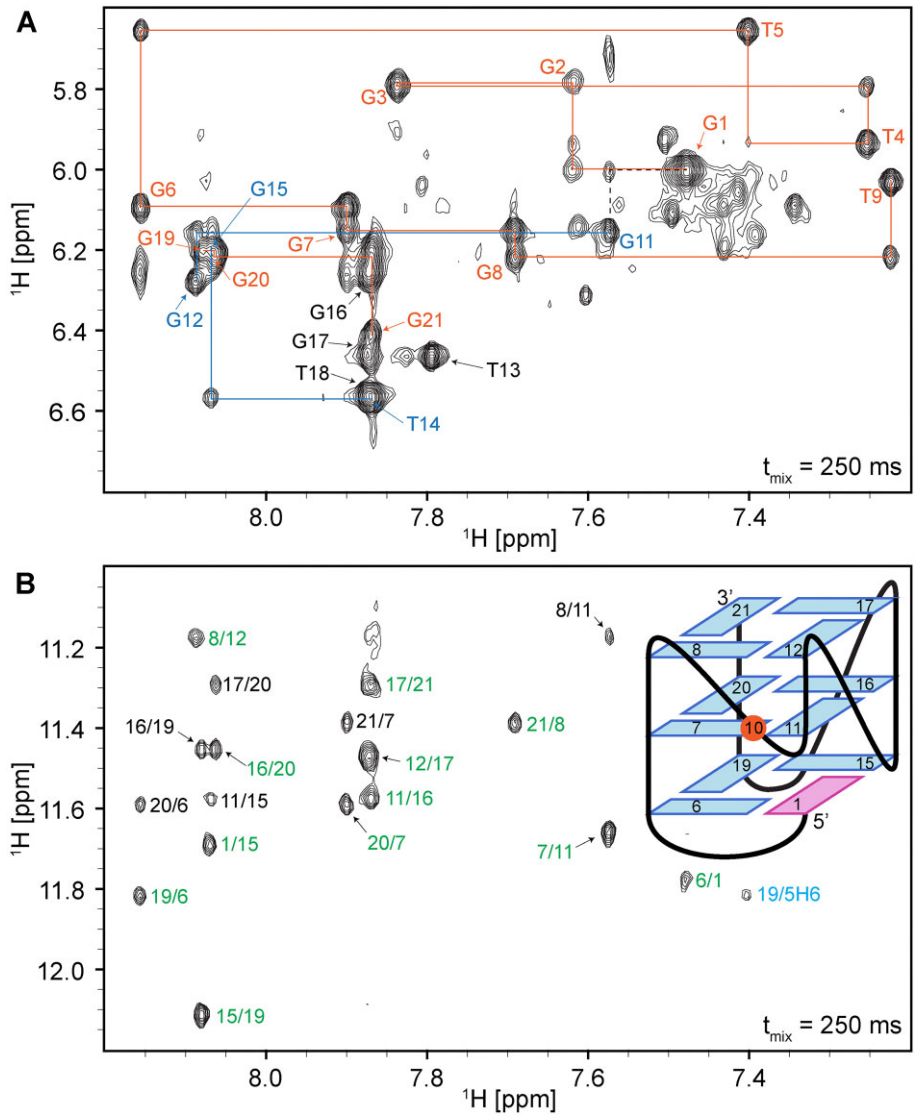

Figure 4. Structure elucidation of the G4 adopted by g10S. (**A**) Aromatic–anomeric region of a NOESY spectrum. Intra-residual H1′–H8 cross-peaks are labeled. Continuous sequential walks are differentiated by color to improve visibility. The nonsequential G1–G11 connectivity is shown with a dashed line. Intra-residual H1′–H8 cross-peaks for which a sequential step was not observed or resolved completely are labeled in black. (**B**) Aromatic–imino region of NOESY spectrum and topological scheme. The inter-residual H1–H8 cross-peaks in the G4 core are labeled green and black for intra- and inter-quartet contacts, respectively. A cross-peak between the core G19 and the stacked loop T5 is labeled in blue. Magenta and blue blocks represent *syn* and *anti* nucleotides, respectively. The oxidative lesion position is marked with an orange circle. Thymine and guanine nucleotides not involved in G-quartets are omitted for clarity. NOESY spectrum was recorded at 5°C on a 600 MHz NMR spectrometer, with a 250 ms mixing time, 0.4 mM DNA, 50 mM KCl, 10 mM potassium phosphate buffer (pH 7), and 10% ^2H_2O.

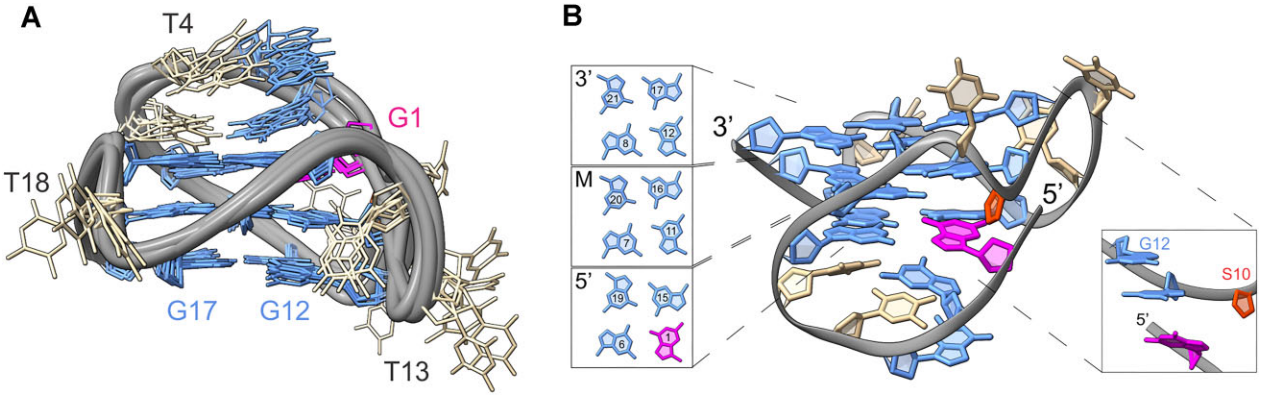

Figure 5. AlphaFold 3 predicted G4 structure adopted by g10S. (**A**) A cluster of five structures in agreement with NMR observables. (**B**) A representative model of g10S highlighting the snapback G1, with top-down views of the three G-quartets.

Table 2. Translational diffusion coefficients of selected G4 species

Construct	Molecularity	Folding protocol	D_t ($\times 10^{-10}$ m^2/s)[a]
g2S	Monomer	Quenched	1.44 ± 0.03
g10S	Monomer	Quenched	1.47 ± 0.03
g19S	Dimer	Annealed	1.17 ± 0.03
Tg19S	Dimer	Annealed	1.18 ± 0.02
	Monomer		1.41 ± 0.03
TTg19S	Monomer	Annealed	1.42 ± 0.02

[a]Translational diffusion coefficients are averages of analysis of signal decay of the resolved aromatic resonances with respective standard deviations.

favoring a monomeric fold at micromolar concentrations. Alternatively, the temperatures for the conversion of dimers to monomers and the unfolding of monomers may be too close to each other to distinguish them experimentally by the UV melting experiment.

In an NMR melting experiment, a dimer-to-monomer conversion would result in a new set of resonances, but none were observed (Supplementary Fig. S22). Therefore, the dimer-to-monomer conversion and monomer unfolding seem to be cooperative. We further investigated the effect of thymine overhangs on the thermal stability of the g19S oligonucleotide. Tg19S and TTg19S with single and double thymine overhangs exhibit single melting transitions at 80 and 77°C, respectively (Supplementary Fig. S14).

The dimeric G19S structure was predicted with AlphaFold 3, with all models having a parallel G4 core and propeller loops. The two G4 units efficiently stack via 5′ G-quartets (Supplementary Fig. S23). Nucleobases G6 and G15 stack with their respective intermolecular counterparts, while G1 stacks with G10, and vice versa. The structure of the 3′ overhang, which includes the displaced G-tract and loop (T18–G21), is dynamic and poorly defined. In the absence of K^+ or in the presence of only five K^+ cations, the 3′ overhang folds back, forcing G20 and G21 to intercalate between G-quartets. Notably, the five K^+ cations are localized within the central cavity but are not equidistantly positioned between G-quartet planes. The best structural predictions were obtained with an ample amount of (50) K^+ cations, where the 3′ overhangs formed capping structures, albeit with poor stacking between nucleobases or with the outer G-quartets (Supplementary Fig. S23). Multiple K^+ cations were localized to the central cavity, with additional cations distributed along the DNA backbone.

Discussion

Promoters and telomeres are GC-rich regions of the (mostly) double-stranded genome. G·C base pairs are thermally very stable and normally guide DNA folding into secondary and tertiary structures, with dsDNA being the commonly favored state. However, G-rich regions of individual strands can also favor G4 formation, influencing the dsDNA:G4 equilibrium. Our experiments on short, 21-nt, two-stranded constructs have shown that single-nucleotide loops connecting G-tracts (mL1) yield stable G4s with almost no dsDNA observed after quenching. In comparison, two-stranded constructs with two- or three-nucleotide loops (mL2 and mL3, respectively) destabilize G4s, favoring dsDNA as the predominant structure. Further tuning of this equilibrium can be achieved by varying individual loop lengths. In mLV, we were able to obtain a balanced ∼1:1 distribution of dsDNA and G4 populations immediately after quenching. The formation of dsDNA depends on the association of two complementary strands and, under *in vitro* conditions, is dependent on the DNA concentration, which is admittedly high in NMR experiments. However, in the genome the two strands are usually in proximity and can readily associate via base pairing. On the other hand, (un)folding of G4s is generally slow and can include multiple intermediate stages. Interconversion between dsDNA and G4 is therefore not a simple two-state process. Our experiments with mLV showed that the initial equilibrium after hybridization is drifting toward dsDNA on a timescale of hours, indicating that dsDNA is the thermodynamically preferred structure. However, a kinetically trapped G4 structure is formed during quenching. A previous study of a two-stranded construct originating from the human telomeric region similarly showed that dsDNA was the preferred state at room temperature [29]. At elevated temperatures, G4 formation accompanied duplex melting. One could arguably diminish the importance of such "transient" G4 structures, but many cellular processes take place on (sub)second timescales and kinetically trapped G4s can be highly populated during these processes.

Oxidative lesions in DNA affect hydrogen bonding, nucleobase stacking, backbone geometry, etc. A single oxidative lesion of guanine can (de)stabilize dsDNA, G4, or both structures. The introduction of **X** or **S** to mLV was not universally detrimental to G4 formation. The preferred state of most two-stranded constructs is dsDNA. However, kinetically trapped G4s were observed for two-stranded constructs with lesions in the first (m1X, m2X, m1S, m2S), third (m10S), and fifth (m19X, m20X, m19S, m20S) G-tracts. Only **S** in the fifth G-tract (m19S, m20S) led to a thermodynamically stable G4 dimer. Interestingly, the three G4 topologies adopted by two-stranded constructs are independent of the type and/or position of the lesion in the G-tract, but rather dependent on which G-tract contains the lesion (Fig. 3D).

The carbonyl group on C8 causes **X** to preferentially adopt the *syn* glycosidic conformation [15]. In this orientation, the Hoogsteen face is exposed and can form the **X**·A wobble base pair. Therefore, mutating the nucleotide opposite **X** to A was expected to stabilize dsDNA and potentially reduce formation of kinetically trapped G4s in our two-stranded constructs. Indeed, the G4 populations in C-to-A mutants were reduced by ∼50% after both quenching and annealing. The somewhat higher population of dsDNA in the mutated two-stranded constructs with respect to fully complementary mixtures can also be attributed to the planar nature of the **X**·A base pair [30]. On the other hand, the out-of-plane **X**·C base pair would destabilize dsDNA. However, recent studies suggest that the **X**·A base pairing considerably populates an extrahelical orientation of **X** in dsDNA [31]. These data could explain why in these two-stranded constructs a small fraction of the conformational space is occupied by G4s, even after annealing.

The presence of five G-tracts in all our two-stranded constructs is crucial for potential replacement of a damaged G-tract. At the outset, we hypothesized that some G-rich strands could adopt kinetically trapped G4s where **X** would participate in G-quartets, as previously observed with the four G-tract human telomeric sequence [19]. In our two-strand constructs, however, **X** is never included in the G4 core. Furthermore, G-rich strands with a single well-defined G4 (g1X, g2X, g19X, and g20X) always rely on the presence of the fifth "spare tire" G-tract to substitute the oxidized G position and

thus maintain the G4 structure. The same effect is observed when the four positions are replaced with **S** as these oligonucleotides (g1S, g2S, g19S, g20S) adopt the same topologies as their **X**-containing counterparts.

The "spare tire" principle operates seamlessly with g2S, effectively bypassing the damaged G-tract while enabling the remaining sequence to form a parallel G4 with propeller-type loops, a topology extensively characterized in the literature [32–34]. A similar displacement of the damaged G-tract was observed in the parallel G4 formed by g19S. However, in this instance, dimerization occurred via end stacking of G-quartets, resulting in the formation of a G4 dimer. Such dimeric structures were previously observed in G4s with propeller loops in which the stacking interface is not sterically hindered by overhangs [35–37].

Interestingly, the "spare tire" is utilized also in the case of g10S, but only partially. Rather than replacing the entire damaged middle G-tract, only **S** is replaced with a single G from the "spare tire," creating a rare 5′-top snapback feature. In such structures, the G-rich sequence folds back on itself forming a snapback loop where the distant 5′ G is brought into proximity of an incomplete 5′ G-quartet. Despite the novel nucleotide sequence and inclusion of an oxidative lesion, a minor subset of predicted G4 structures adopted by g10S using AlphaFold 3 are in agreement with our NOE cross-peak assignments and proposed topology. This points to the convenience of computational prediction tools in forecasting nucleic acid structure when used in conjunction with experimental data. Two cases of 5′-top snapback G4s have been reported to date. In the first, an isolated 5′ G completes a hybrid-type G4 derived from the telomeric DNA of *Tetrahymena thermophila* [38]. In the second known example, the snapback loop forms a short double-helical segment, with the 5′ G inserted into the G-quartet at the G4–duplex interface [39]. However, in our case, the snapback topology of g10S is disrupted when the strand is extended in the 5′ direction. While the resulting G4 retains three G-quartet planes, perturbations in the NMR resonances suggest the formation of an alternative topology (Supplementary Fig. S7).

The thermal stability of G4s is primarily influenced by the loop length, with the highest stability observed for those with loops with a single nucleotide [40, 41]. This is in line with our two-stranded constructs mL1, mL2, and mL3, where longer loops result in reduced G4 populations and favor duplex structures. Among the studied two-stranded constructs, g2S, g10S, and g19S exhibit exceptionally high thermal stability, forming G4 structures with melting temperatures ranging from 67 to 86°C. These values exceed the melting temperature of the mLV two-stranded constructs (65°C). This behavior is consistent with prior observations in which G4s derived from the human telomeric sequence displayed higher melting temperatures than their hybridized dsDNA counterparts, despite dsDNA being the preferred state [42, 43].

Oxidative damage is not the only factor affecting kinetics and equilibria between different secondary structures. Other cellular processes, such as downstream base excision repair steps, can promote G4 folding. For example, strand scission relaxes structural constraints in duplex DNA, enhancing G4 formation. Furthermore, the presence of G4-binding proteins can promote the folding of a G-rich region into a G4 structure, even when nested within a dsDNA region [44]. Since oxidative damage, repair mechanisms, and G4 folding are dynamic cellular processes, it is plausible that kinetically trapped G4s form during genomic events such as DNA unwinding [45, 46]. These events may interfere with enzymatic processes essential for genomic maintenance, affecting DNA replication and transcription, particularly in promoter regions. Our findings shed light on how oxidative damage influences the dsDNA:G4 equilibrium and provide a foundation for further studies into the roles and functions of nucleic acids under oxidative stress conditions.

Acknowledgements

This project is part of the Ph.D. "Structural changes of oxidized guanine-rich genomic regions" supported by CERIC-ERIC.

Author contributions: Simon Aleksič (Data curation [equal], Formal analysis [equal], Investigation [equal], Visualization [equal], Writing—original draft [equal], Writing—review & editing [equal]), Peter Podbevšek (Conceptualization [equal], Data curation [equal], Formal analysis [equal], Investigation [equal], Visualization [equal], Writing—original draft [equal], Writing—review & editing [equal]), and Janez Plavec (Conceptualization [equal], Funding acquisition [equal], Project administration [equal], Supervision [equal], Validation [equal], Writing—original draft [equal], Writing—review & editing [equal])

Supplementary data

Supplementary data is available at NAR online.

Conflict of interest

None declared.

Funding

This work was funded by the Slovenian Research and Innovation Agency (ARIS) (grant numbers P1-0242 and J1-60019) and CERIC-ERIC through a Ph.D. grant to S.A. Funding to pay the Open Access publication charges for this article was provided by the Slovenian Research and Innovation Agency (ARIS) (grant numbers P1-0242 and J1-60019).

Data availability

NMR spectra are deposited in Zenodo (https://doi.org/10.5281/zenodo.14261288).

References

1. Marsico G, Chambers VS, Sahakyan AB *et al.* Whole genome experimental maps of DNA G-quadruplexes in multiple species. *Nucleic Acids Res* 2019;**47**:3862–74. https://doi.org/10.1093/nar/gkz179
2. Prorok P, Artufel M, Aze A *et al.* Involvement of G-quadruplex regions in mammalian replication origin activity. *Nat Commun* 2019;**10**:3274. https://doi.org/10.1038/s41467-019-11104-0
3. Chen Y, Simeone A, Melidis L *et al.* An upstream G-quadruplex DNA structure can stimulate gene transcription. *ACS Chem Biol* 2024;**19**:736–42. https://doi.org/10.1021/acschembio.3c00775
4. Mendoza O, Elezgaray J, Mergny JL. Kinetics of quadruplex to duplex conversion. *Biochimie* 2015;**118**:225–33. https://doi.org/10.1016/j.biochi.2015.09.031

5. Grün JT, Blümler A, Burkhart I *et al.* Unraveling the kinetics of spare-tire DNA G-quadruplex folding. *J Am Chem Soc* 2021;**143**:6185–93. https://doi.org/10.1021/jacs.1c01089
6. Hud NV, Plavec J. The role of cations in determining quadruplex structure and stability. In: Neidle S, Balasubramanian S (eds.), *Quadruplex Nucleic Acids*. Cambridge: Royal Society of Chemistry, 2006, 100–30.
7. Dvorkin SA, Karsisiotis AI, Webba da Silva M. Encoding canonical DNA quadruplex structure. *Sci Adv* 2018;**4**:eaat3007. https://doi.org/10.1126/sciadv.aat3007
8. Farag M, Messaoudi C, Mouawad L. ASC-G4, an algorithm to calculate advanced structural characteristics of G-quadruplexes. *Nucleic Acids Res* 2023;**51**:2087–107. https://doi.org/10.1093/nar/gkad060
9. Kasai H, Nishimura S. Hydroxylation of deoxyguanosine at the C-8 position by ascorbic acid and other reducing agents. *Nucleic Acids Res* 1984;**12**:2137–45. https://doi.org/10.1093/nar/12.4.2137
10. Fleming AM, Zhu J, Howpay Manage SA *et al.* Human NEIL3 gene expression regulated by epigenetic-like oxidative DNA modification. *J Am Chem Soc* 2019;**141**:11036–49. https://doi.org/10.1021/jacs.9b01847
11. Klungland A, Rosewell I, Hollenbach S *et al.* Accumulation of premutagenic DNA lesions in mice defective in removal of oxidative base damage. *Proc Natl Acad Sci USA* 1999;**96**:13300–5. https://doi.org/10.1073/pnas.96.23.13300
12. Kumar N, Theil AF, Roginskaya V *et al.* Global and transcription-coupled repair of 8-oxoG is initiated by nucleotide excision repair proteins. *Nat Commun* 2022;**13**:974. https://doi.org/10.1038/s41467-022-28642-9
13. Wilson DM, Barsky D. The major human abasic endonuclease: formation, consequences and repair of abasic lesions in DNA. *Mutat Res* 2001;**485**:283–307. https://doi.org/10.1016/S0921-8777(01)00063-5
14. Vesnaver G, Chang CN, Eisenberg M *et al.* Influence of abasic and anucleosidic sites on the stability, conformation, and melting behavior of a DNA duplex: correlations of thermodynamic and structural data. *Proc Natl Acad Sci USA* 1989;**86**:3614–8. https://doi.org/10.1073/pnas.86.10.3614
15. Singh SK, Szulik MW, Ganguly M *et al.* Characterization of DNA with an 8-oxoguanine modification. *Nucleic Acids Res* 2011;**39**:6789–801. https://doi.org/10.1093/nar/gkr275
16. Crenshaw CM, Wade JE, Arthanari H *et al.* Hidden in plain sight: subtle effects of the 8-oxoguanine lesion on the structure, dynamics, and thermodynamics of a 15-base pair oligodeoxynucleotide duplex. *Biochemistry* 2011;**50**:8463–77. https://doi.org/10.1021/bi201007t
17. Bielskutė S, Plavec J, Podbevšek P. Oxidative lesions modulate G-quadruplex stability and structure in the human BCL2 promoter. *Nucleic Acids Res* 2021;**49**:2346–56. https://doi.org/10.1093/nar/gkab057
18. Esposito V, Martino L, Citarella G *et al.* Effects of abasic sites on structural, thermodynamic and kinetic properties of quadruplex structures. *Nucleic Acids Res* 2010;**38**:2069–80. https://doi.org/10.1093/nar/gkp1087
19. Bielskutė S, Plavec J, Podbevšek P. Impact of oxidative lesions on the human telomeric G-quadruplex. *J Am Chem Soc* 2019;**141**:2594–603. https://doi.org/10.1021/jacs.8b12748
20. Rossiello F, Jurk D, Passos JF *et al.* Telomere dysfunction in ageing and age-related diseases. *Nat Cell Biol* 2022;**24**:135–47. https://doi.org/10.1038/s41556-022-00842-x
21. Revy P, Kannengiesser C, Bertuch AA. Genetics of human telomere biology disorders. *Nat Rev Genet* 2023;**24**:86–108. https://doi.org/10.1038/s41576-022-00527-z
22. Alanazi AFR, Parkinson GN, Haider S. Structural motifs at the telomeres and their role in regulatory pathways. *Biochemistry* 2024;**63**:827–42. https://doi.org/10.1021/acs.biochem.4c00023
23. Karimian K, Groot A, Huso V *et al.* Human telomere length is chromosome end-specific and conserved across individuals. *Science* 2024;**384**:533–9. https://doi.org/10.1126/science.ado0431
24. Fleming AM, Zhou J, Wallace SS *et al.* A role for the fifth G-track in G-quadruplex forming oncogene promoter sequences during oxidative stress: do these 'spare tires' have an evolved function? *ACS Cent Sci* 2015;**1**:226–33. https://doi.org/10.1021/acscentsci.5b00202
25. Abramson J, Adler J, Dunger J *et al.* Accurate structure prediction of biomolecular interactions with AlphaFold 3. *Nature* 2024;**630**:493–500. https://doi.org/10.1038/s41586-024-07487-w
26. Pavc D, Wang B, Spindler L *et al.* GC ends control topology of DNA G-quadruplexes and their cation-dependent assembly. *Nucleic Acids Res* 2020;**48**:2749–61. https://doi.org/10.1093/nar/gkaa058
27. Pavc D, Sebastian N, Spindler L *et al.* Understanding self-assembly at molecular level enables controlled design of DNA G-wires of different properties. *Nat Commun* 2022;**13**:1062. https://doi.org/10.1038/s41467-022-28726-6
28. del Villar-Guerra R, Trent JO, Chaires JB. G-quadruplex secondary structure obtained from circular dichroism spectroscopy. *Angew Chem Int Ed* 2018;**57**:7171–5. https://doi.org/10.1002/anie.201709184
29. Phan AT, Mergny JL. Human telomeric DNA: G-quadruplex, i-motif and Watson–Crick double helix. *Nucleic Acids Res* 2002;**30**:4618–25. https://doi.org/10.1093/nar/gkf597
30. Reynisson J, Steenken S. The calculated base pairing energy of 8-oxoguanine in the *syn–anti* conformation with cytosine, thymine, adenine and guanine. *J Mol Struct THEOCHEM* 2005;**723**:29–36. https://doi.org/10.1016/j.theochem.2004.12.014
31. Ovcherenko SS, Shernyukov AV, Nasonov DM *et al.* Dynamics of 8-oxoguanine in DNA: decisive effects of base pairing and nucleotide context. *J Am Chem Soc* 2023;**145**:5613–7. https://doi.org/10.1021/jacs.2c11230
32. Parkinson GN, Lee MPH, Neidle S. Crystal structure of parallel quadruplexes from human telomeric DNA. *Nature* 2002;**417**:876–80. https://doi.org/10.1038/nature755
33. Phan AT, Modi YS, Patel DJ. Propeller-type parallel-stranded G-quadruplexes in the human c-myc promoter. *J Am Chem Soc* 2004;**126**:8710–6. https://doi.org/10.1021/ja048805k
34. Agrawal P, Hatzakis E, Guo K *et al.* Solution structure of the major G-quadruplex formed in the human VEGF promoter in K^+: insights into loop interactions of the parallel G-quadruplexes. *Nucleic Acids Res* 2013;**41**:10584–92. https://doi.org/10.1093/nar/gkt784
35. Do NQ, Lim KW, Teo MH *et al.* Stacking of G-quadruplexes: NMR structure of a G-rich oligonucleotide with potential anti-HIV and anticancer activity. *Nucleic Acids Res* 2011;**39**:9448–57. https://doi.org/10.1093/nar/gkr539
36. Kuryavyi V, Cahoon LA, Seifert HS *et al.* RecA-binding *pilE* G4 sequence essential for pilin antigenic variation forms monomeric and 5′ end-stacked dimeric parallel G-quadruplexes. *Structure* 2012;**20**:2090–102. https://doi.org/10.1016/j.str.2012.09.013
37. Adrian M, Ang DJ, Lech CJ *et al.* Structure and conformational dynamics of a stacked dimeric G-quadruplex formed by the human CEB1 minisatellite. *J Am Chem Soc* 2014;**136**:6297–305. https://doi.org/10.1021/ja4125274
38. Beseiso D, Chen EV, McCarthy SE *et al.* The first crystal structures of hybrid and parallel four-tetrad intramolecular G-quadruplexes. *Nucleic Acids Res* 2022;**50**:2959–72. https://doi.org/10.1093/nar/gkac091
39. Lim KW, Phan AT. Structural basis of DNA quadruplex–duplex junction formation. *Angew Chem Int Ed* 2013;**52**:8566–9. https://doi.org/10.1002/anie.201302995
40. Guédin A, Gros J, Alberti P *et al.* How long is too long? Effects of loop size on G-quadruplex stability. *Nucleic Acids Res* 2010;**38**:7858–68. https://doi.org/10.1093/nar/gkq639
41. Kumar N, Sahoo B, Varun KAS *et al.* Effect of loop length variation on quadruplex–Watson Crick duplex competition.

Nucleic Acids Res 2008;**36**:4433–42. https://doi.org/10.1093/nar/gkn402
42. Salazar M, Thompson BD, Kerwin SM *et al.* Thermally induced DNA·RNA hybrid to G-quadruplex transitions: possible implications for telomere synthesis by telomerase. *Biochemistry* 1996;**35**:16110–5. https://doi.org/10.1021/bi961442j
43. Chalikian TV, Liu L, Macgregor RB. Duplex–tetraplex equilibria in guanine- and cytosine-rich DNA. *Biophys Chem* 2020;**267**:106473. https://doi.org/10.1016/j.bpc.2020.106473
44. Fleming AM, Guerra Castañaza Jenkins BL, Buck BA *et al.* DNA damage accelerates G-quadruplex folding in a duplex–G-quadruplex–duplex context. *J Am Chem Soc* 2024;**146**:11364–70. https://doi.org/10.1021/jacs.4c00960
45. Lan L, Nakajima S, Oohata Y *et al. In situ* analysis of repair processes for oxidative DNA damage in mammalian cells. *Proc Natl Acad Sci USA* 2004;**101**:13738–43. https://doi.org/10.1073/pnas.0406048101
46. Summers PA, Lewis BW, Gonzalez-Garcia J *et al.* Visualising G-quadruplex DNA dynamics in live cells by fluorescence lifetime imaging microscopy. *Nat Commun* 2021;**12**:162. https://doi.org/10.1038/s41467-020-20414-7

Received: December 3, 2024. **Revised:** March 17, 2025. **Editorial Decision:** March 20, 2025. **Accepted:** March 21, 2025